Materials & Design 242 (2024) 112994

Contents lists available at ScienceDirect

Materials & Design

journal homepage: www.elsevier.com/locate/matdes

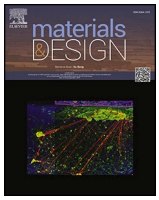

Probing local adhesion: A miniaturized multi-photon lithography design demonstrated on silanized vs. untreated surfaces

Alexander Jelinek [a,*], Elisabeth Rossegger [b], Sandra Schlögl [b], Daniel Kiener [a], Markus Alfreider [a]

[a] Department of Materials Science, Montanuniversität Leoben, Franz Josef-Straße 18, 8700 Leoben, Austria
[b] Polymer Competence Center Leoben GmbH, Sauraugasse 1, 8700 Leoben, Austria

ARTICLE INFO

Keywords:
Multi-photon lithography
Adhesion
Tensile specimen
Micromechanics
Photoresist

ABSTRACT

As multi-photon lithography technology matures, advanced integrated device design concepts become possible, positioned onto small surfaces, such as optical fibres. Only local adhesion anchors the printed object on the surface and ensure proper print-development without structure loss and long-term usability. Although surface treatments such as silanization are well known to considerably increase adhesion strength, quantification of adhesion is not straightforward and commonly assessed indirectly by surface characteristics and technological methods. The present work aims to quantify adhesion on a micrometer scale through SEM *in situ* tension experiments, that utilize a newly developed specimen geometry. Multiple specimens, with various footprints, were manufactured on both silanized and untreated fused silica substrates, allowing the comparable quantification of adhesion stresses between different surface conditions. Specimens on an untreated substrate failed with a high scatter in detaching force, whereas specimens on a silanized substrate tend to fail within the photoresist, either at the gauge section or just above the substrate, rather than at the interface itself. Thus, the adhesion stress was increased at least by a factor of 1.4 by the silanization treatment. Generally, a novel approach was developed, that can quantify local adhesions properties in realistic packaging or integrated circuits.

1. Introduction

Multi-photon lithography (MPL) based on multi-photon polymerization enables direct laser writing, with precision even below the resolution limit of visible light [1–3]. It is a free-form manufacturing technique suitable for use at the micro- and nanoscale, without the need for common lithographical steps such as spin coating, etching or stripping. Thanks to recent developments regarding usability – primarily commercial printer systems enabling straightforward manufacturing of complex objects from a digital blueprint – this miniaturized device design is now accessible for a broad variety of scientific fields [4–7]. Common printer platforms utilize a light microscope-like setup, with different objectives for high and low magnification focusing, therefore allowing precise alignment of printed structures with features of the substrate via a live-view feature. This feature is crucial for aligning fluid manipulation devices within microfluidic paths [8,9], printing devices for cell manipulation [10,11], writing photonic waveguides [12–14] coupled with chips [15–19] or manufacturing on top of optical fibres [20–23]. Although the process is limited by the available photoresists, new formulations are being developed to finally use different materials such as hydrogels [24], ceramics [25–28], metals [29–33] or fused silica [34], using either particles fillings or special photoresists formulations [7,14].

However, during application, major issues arise from many steps in the printing process – e.g. as large overhanging features, shrinkage due to curing of the resin, swelling during development [35,36], and poor adhesion towards the printing substrate. While unsupported overhangs and shrinkage can be systematically accounted for during device design by iterative adaptations [37], the adhesion strength is predefined by the resin-substrate pairing and can only be externally altered by surface treatments. If the structure's adhesion strength cannot withstand liquid flow within the development bath, solvent capillary forces and shrinkage, detaching will occur. Although partial detachments can also be used beneficially [38], fully detached MPL structures usually get lost due to their small size. Thus, a vast majority of small-scale applications rely on perfect local adhesion towards the substrate [14,39–42]. This is especially true for reliable miniaturized device manufacturing, as structures should occupy target positions such as fibre cross sections, fluid wells, or silicon chip positions, with specific surface properties and, potentially, load-bearing capabilities. To tackle this issue, a

* Corresponding author.
E-mail address: alexander.jelinek@unileoben.ac.at (A. Jelinek).

https://doi.org/10.1016/j.matdes.2024.112994
Received 14 March 2024; Received in revised form 28 April 2024; Accepted 29 April 2024
Available online 30 April 2024

quantitative, reliable rating of adhesion is necessary to design a systematic development process and improve adhesion on local regions of interest. Until now, mechanical adhesion measurements are dominated by qualitative indirect methods (e.g. structure loss [36], tape pull of tests, indentation buckling, etc.). A method for spatially localised quantitative adhesion testing would complement shear-based methods [43,44] and facilitate data acquisition on experiments performed directly on the materials of interest. Thus, the first aim of the presented work is the development of a novel methodology, which enables adhesion testing on a very localized spot. The same process of devising manufacturing with MPL is used for adhesion specimen testing. The identical photoresist material can therefore be used, assuring that the results of the adhesion analysis can be directly applied on the targeted device substrate. The second aim of this work is a comparison of differently treated surfaces to demonstrate the application of the adhesion measurement method. Therefore, a general improvement of adhesion through the treatment is desired, and the selected treatment should be relevant for existing applications, such as tailored adhesive structures themselves [45–49] or imprint lithography masks [42,45,50], in case if post-treatment steps as pyrolysis [43] or infiltration [51] are intended.

Roughening of the substrate surface, which introduces mechanical interlocking sites, is usually not desired, due to the small manufacturing dimensions and resulting geometric artefacts which might arise. Generally, the combination of different materials, such as a photoresist on one side and polished fused silica or silicon on the other, show no external force mediating covalent bonds at the interface, leaving only weak *van der Waals* forces to mediate interaction. Consequently, surface functionalization of the substrate, by means of introducing specific chemical bounding sites, is a promising way to overcome this issue [42,43].

This surface functionalization treatment, as carried out, is depicted in Fig. 1 (green section). Before the actual functionalization step, a prior activation step via a non-thermal plasma treatment (e.g. by dielectric barrier discharge or corona discharge) is commonly applied to efficiently remove carbon-containing residues and create binding moieties (mainly hydroxylic groups) on of the fused silica surface [52,53]. Next, a reactive group is covalently bound to these moieties. In the case of silicon or fused silica in combination with an acrylic photoresist, a silane containing acrylate or methacrylate groups is suitable to form stable Si – O – Si – R bonds [43,54] from OH – groups. Conveniently, the reaction can be performed by simple immersion of the substrate into a solution containing a suitable reactive agent at an elevated temperature, followed by a baking step. Finally, the now exposed acrylate moieties participate in the polymerization reaction during MPL, although immobilized on the substrate surface. Consequently, superior adhesion of the whole print is achieved by covalently connecting the structure to the substrate.

In a previous work, a sheer testing approach was applied to polymer cubes of varied side lengths to measure the shear stress and adhesion energy [43] and thereby facilitate a comparison between treated and

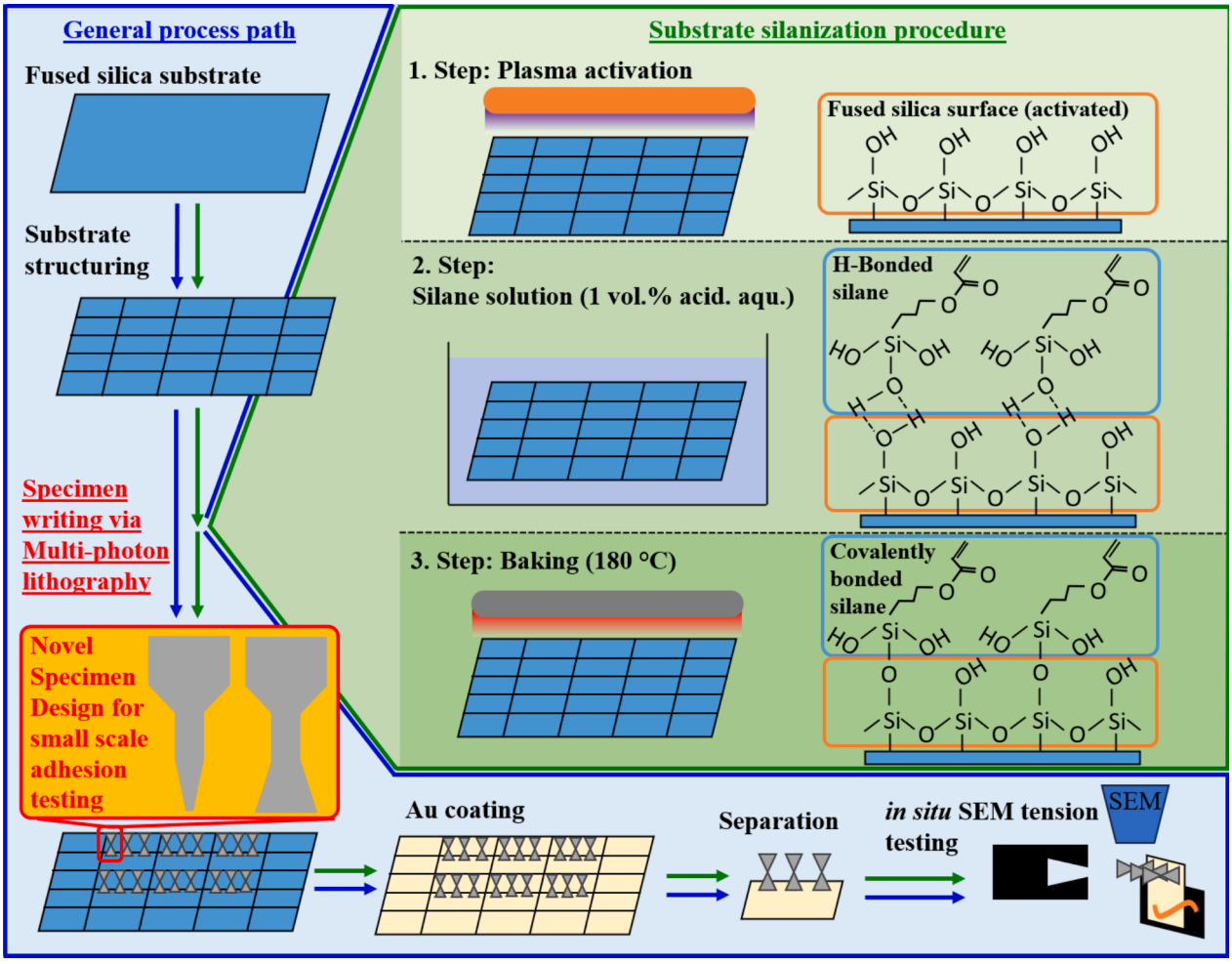

Fig. 1. A novel specimen design to facilitate small scale adhesion testing. For showcasing the testing methodology, two major experimental paths were conducted to assess the adhesion strength's increase due to a silanization treatment. One specimen set was manufactured on a treated (green path) and another on an untreated (blue path) fused silica substrate. With exception of the three-step silanization treatment, the same steps were performed, starting from the pristine substrate, followed by structuring, specimen manufacturing, application of a conductive coating, specimen separation, and finally *in situ* SEM tension experiments.

untreated substrates. In this current work, we present a new characterisation method to directly access the adhesion force perpendicular to the substrate by utilizing the fabrication abilities of MPL. A specialized, tuneable tension geometry was used to determine the normal stresses required for the detachment of the specimens from the printing substrate. To rationalize the effect of a silanization procedure, a direct comparison of a treated vs. untreated substrate was made. Fig. 1 (blue section) depicts a sketch of the two experimental paths taken to facilitate such a comparison.

A commonly used MPL-photoresist/substrate combination (IP-DIP by NanoScribe GmbH on fused silica) was investigated based on the specifications for NanoScribe's printer devices [55]. The resin IP-DIP had the highest resolution possible on the available device as well as practical relevance for MPL devices [11,12,15–18,23,33,36,42,44,49,50,56–58]. Further, a certain number of literature sources already documented mechanical properties [40,43,58–60] of the IP-DIP-derived polymer, allowing for literature comparison. In regards to the substrate, fused silica is one standard material for MPL printing [3,4,10,17,19,23,25,28,43,44,47,52,58,61]. Additionally, its surface is chemically similar to common silica or borosilicate glass. Automated manufacturing of mechanical specimens was utilized to generate a specimen set with various footprint sizes, enabling insight into the possible influence of contact area on adhesion strength, and reducing the effort of iteratively identifying a suitable footprint size. An area range of ~ 10 to 450 μm^2 was chosen, which is representative of microscale objects able to be to be printed by a MPL device onto target positions, such as an optical fibre cross section. The size regime of the specimens required *in situ* testing within a scanning electron microscope (SEM) to accurately position the gripper within a few tens of nm. A fixed displacement rate was applied during testing to measure the resulting tension force. Further, the images obtained during specimen loading allowed additional information to be collected for the verification and interpretation of mechanical results. Multiple experiments on nominally identical specimen geometries were performed to add a reproducibility check to the overall assessment. A similar series of experiments were performed on the silanized and untreated substrates for comparison, allowing the quantification of the effect of pre-treatment on adhesion.

2. Experimental

2.1. Specimen design

The specimen geometry, shown in Fig. 2(a) to (c), was designed to fit the dimension of the tension specimen gripper of the testing setup, leaving just enough space for manual mounting. Below the head and the gauge section, which have constant dimensions, there is an expansion or narrowing of the cross section towards a square shaped footprint, with individual side length of a. To vary the adhesion area, 14 different values for a, between 2 μm and 26 μm, were selected and the digital geometry (".stl"-file) was generated using the automatization capabilities of the open source software FreeCAD (version: 0.18).

2.2. Substrate preparation and silaniziation

For printing substrates, standard fused-silica platelets (Nanoscribe GmbH & Co. KG, Eggstein-Leopoldshafen, Germany) with lateral dimensions of $1'' \times 1''$ and 725 μm thickness were prepared for eventual splitting and mounting within the SEM *in situ* testing setup [39]. Grooves, ~ 350 μm deep, were applied parallel to the substrate edges in a grid shape with 5 × 5 mm^2 sections using a diamond wire saw (type: 6234, well Diamantdrahtsägen GmbH, Mannheim, Germany). Afterwards, the pieces were cleaned using detergent water and degreased with isopropanol in an ultrasonic bath. The prepared substrates were used with or without surface silanization. For the silanization procedure, an non-thermal plasma activation was conducted with a corona-plasma device (custom built, Ahlbrandt System GmbH, Lauterbach, Germany),

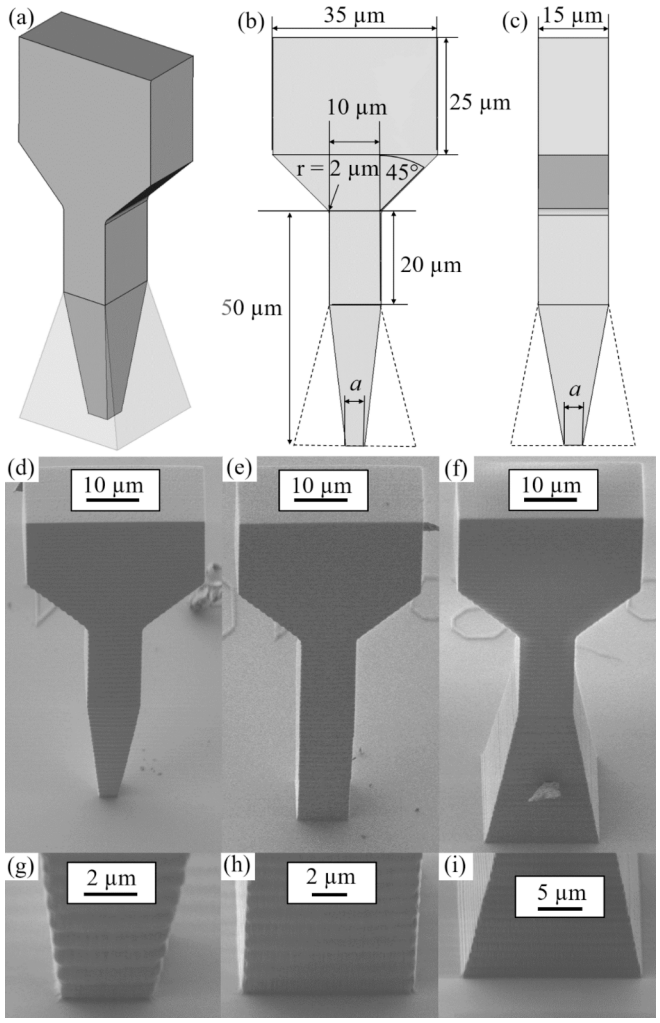

Fig. 2. (a) Schematics of the specimen shapes used, consisting of a head for gripping and a pyramidal changing base for alteration of the adhesion surface. (b) Front view and (c) side view of the digital model, including nominal dimensions. Actual dimensions will deviate from the indicated values due to shrinkage. (d), (g) Printed specimen with smaller adhesion area than the gauge cross section, (e), (h) with nearly straight shape, and (f), (i) with larger footprint than the gauge cross section, respectively.

directly followed by submersion in the silan solution (27 mL ethanol (100 %), 3 mL deionized water, 5 drops of glacial acetic acid and 300 μL 3-(trimethoxysilyl)propyl acrylate) for 24 h at 70 °C in a sealed Petri dish. After that, the substrate was rinsed with ethanol and dried before baking at 180 °C for 8 h [54]. Until printing, the substrates were dry stored in a desiccator at room temperature.

2.3. Surface energy measurement

For comparison, the surface energies, γ, of the photoresist (IP-DIP from Nanoscribe GmbH & Co. KG, Eggstein-Leopoldshafen, Germany), both the untreated and silanized substrates, were determined via the standardized Owens-Wendt method [62], based on contact angle measurements towards 1 μL droplets of water and diiodomethane. To achieve this, a dosing apparatus with a low magnification digital light microscope (DSA 100-HT400, Krüss GmbH, Hamburg, Germany) was employed, including the corresponding software. A 2–5 μm thin layer of the IP-DIP was printed on a fused silica substrate, spreading over a few mm^2 to enable the deposition of liquid drops and contact angle measurements. Additionally, the surface energy for the gold coating on the substrate was found for verifying the measurements.

2.4. Direct laser writing of tension specimens

For the specimen printing via multi-photon lithography, a device (Photonic Professional GT2, NanoScribe GmbH & Co. KG, Eggstein, Leopoldshafen, Germany) with a 63× objective (Plan-APOCHROMAT 63× N.A. 1.4 Oil DIC, Carl Zeiss AG, Oberkochen, Germany) and a standard negative-tone photoresist IP-DIP (Nanoscribe GmbH & Co. KG, Eggstein-Leopoldshafen, Germany) were employed. The CAD models were sliced with 100 nm and hatched with 200 nm, with the hatching direction was rotated by 90° between layers. The writing was performed with a standard 10 mm/s writing speed and 20 mW laser power, corresponding to a laser power parameter of 40. Every print was started 500 nm below the substrate interface, identified via the auto-focusing feature of the system, to avoid floating parts. A specimen set was defined via a writing script – containing all 14 actual and 8 dummy specimens (for tungsten grip cleaning) in a row with an intermediate spacing of 200 μm – and an additional sample labelling text indicating the individual adhesion area width a for more convenient evaluation. Such sets were printed about 50 μm apart from (but parallel to) a sawing groove. Finally, two or three sets of specimens were fabricated on an untreated or silanized substrate, respectively.

To increase the SEM image quality, the substrates (including the specimens) were coated with a conductive gold layer a few nanometers thickness by a sputter coater (Sputter Coater 108auto, Cressington Scientific Instruments Ltd., Watford, UK). A hard metal scriber was used to scratch along the sawing grooves in the substrate, thus introducing a pre-crack for the splitting of the substrate partitions. A self-made gripping tool (made via fused filament printing out of polylactic acid) facilitated clamping of the substrate near a pre-scratched groove as the loose part was carefully manually bent to break the partitions apart in a controlled manner. A row of three 5 × 5 mm^2 sections, each holding one set of specimens, was then mounted via a conductive leaf spring for consecutive SEM *in situ* testing.

2.5. SEM in situ testing

The mechanical tension testing was performed via an inherently displacement-controlled *in situ* nanoindenter (UNAT-SEM 1, ASMEC GmbH, Dresden, Germany) in open-loop mode within an SEM (LEO 982, Carl Zeiss AG, Oberkochen, Germany) using a tungsten grip [63,64]. All experiments were conducted at room temperature and under common SEM vacuum conditions (~ 10^{-6} mbar). After mounting an individual specimen under continuous imaging (acceleration voltage: 3 kV), a tensile load was applied with a constant displacement rate of 100 nm/s until the specimen failed. During the experiments, two SEM images were recorded per second for subsequent analysis.

The global strain rate of the experiment could be estimated for the initial specimen length of ~ 50 μm and uniform cross section as ~ $2 * 10^{-3}$ s^{-1}. The locally prevailing strain rate strongly depends on the cross-section evolution along base and gauge section, as thinner parts accumulate more of the total strain relative to thicker ones. A detailed strain rate evolution for the various specimen shapes might be obtained by finite element simulation, or extracted from specifically patterned specimens using digital image correlation [64]. However, these measurements are outside the scope of this paper.

3. Results

The surface energy results, determined via the Owens-Wendt method, are summarized in Table 1. The polar energy contributions, $\gamma_{surface,\ polar}$, increased by about 80 % (from 4.1 to 7.5 mJ/m^2) during the silanization procedure, whereby the disperse portion of the surface energy, $\gamma_{surface,\ disperse}$, increased only slightly, from 40 to 41 mJ/m^2. The printed photoresist IP-DIP shows nearly the same $\gamma_{surface,\ disperse}$ as the silanized substrate, but a $\gamma_{surface,\ polar}$ of 1.3 mJ/m^2, which is considerably smaller than both substrate conditions. Thus, the overall difference in surface energy $\gamma_{surface,\ total}$ of all three surfaces is mainly caused by a change of the polar energy contribution. Izard *et al.* [43] previously reported values for $\gamma_{surface,\ total}$ with only 1 mJ/m^2 difference for both substrate conditions, in good agreement with presented values, but the total surface energy of IP-DIP is considerably lower at 37.7 mJ/m^2. The surface energy of gold, of 50 mJ/m^2, was mainly determined from the disperse contribution, but agrees well with values from literature [65,66]. It is worth noting that absolute values are strongly influenced by the method used and superficial surface condition as roughness, contamination, treatments etc.

Table 1
Surface energies of all relevant surfaces, including discrimination between disperse and polar contributions.

Surface	$\gamma_{surface,\ disperse}$ [mJ/m^2]	$\gamma_{surface,\ polar}$ [mJ/m^2]	$\gamma_{surface,\ total}$ [mJ/m^2]
Untreated substrate	40.0 ± 0.4	4.1 ± 0.3	**44.1 ± 0.7**
Silanized substrate	40.9 ± 0.4	7.5 ± 0.3	**48.4 ± 0.7**
IP-DIP photoresist	41.1 ± 0.9	1.3 ± 0.2	**42.4 ± 1.0**
Au coated substrate	50.0 ± 0.8	0.08 ± 0.02	**50.0 ± 0.8**

As illustrated in Fig. 3, three distinct failure modes were evident in the tension experiments: failure near the specimen's head (Fig. 3(a,b)), failure close to the polymer-substrate interface (Fig. 3(c,d)), and complete detachment from the substrate (Fig. 3(e,f)). For further discussion in graphs, these modes shall be distinguished by markers as shown in the upper corners of Fig. 3(b), (d) and (f), respectively. Filled markers indicate failure at or near the base while empty ones correspond to gauge failure. Triangular or star-shaped markers are reserved for force, and square markers for stress plotting.

Fig. 3(a) shows a representative specimen which failed critically within the gauge section towards the specimen head, with the resulting fracture surface shown in (b). Generally, this occurs if the polymer-substrate adhesion is sufficient to sustain the loading until the polymer fails at the most critical position of the specimen. This failure mode corresponds to "common" tension testing on straight or dogbone shaped specimens, where the failure force is determined by bulk material properties.

When examining failure near the interface, treated and untreated substrates must be looked at separately. Fig. 3(c) shows the case of a silanized substrate, where cracking occurred very near, but not directly at, the interface. As is apparent in (c) (red encircled area), a portion of the first layers remained attached to the substrate surface. In nearly every case, polymer remnant covered the whole fracture surface, as evident in Fig. 3(d). A few individual specimens displayed a small part of the flat substrate surface below the fracture (green encircled region in (d)), suggesting very similar thresholds for adhesive and cohesive failure at the local level [67]. This failure behavior appeared for all specimens with a silanized adhesion surface and a cross-sectional area equal to or smaller than the gauge cross section.

This behavior is strongly contrasted by the untreated substrate, (e). Here, a complete detachment occurred directly at the polymer-substrate interface, with no material remaining on the substrate surface, leaving a perfectly flat imprint, as depicted in (f). With increasing surface adhesion, no distinct transition point from surface detachment to specimen failure, similar to (a), could be determined. Individual specimens of every adhesion surface area were observed to fail via complete detachment from untreated substrates, suggesting a high stochasticity in the local adhesion.

Fig. 4 shows load vs. displacement graphs of selected tension experiments on (a) silanized and (b) untreated substrates. For every specimen footprint size, one representative dataset is plotted, with exception of the smallest one (a ~ 2 μm), which detached from the

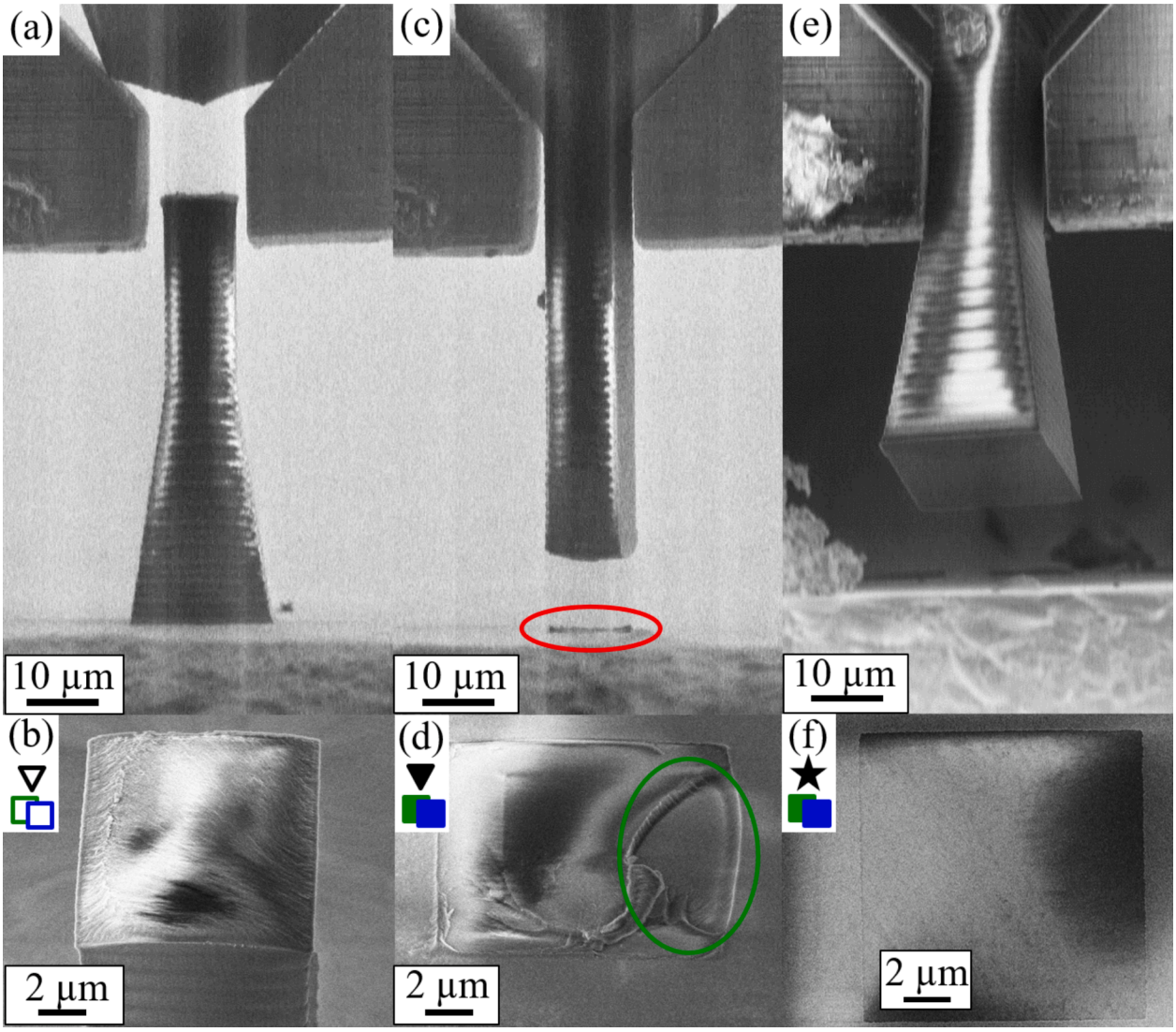

Fig. 3. Failure modes occurring during the tension tests. (a) Failure within the most critical part of the gauge section near the specimen head. Sufficient adhesion to the substrate enabled the common failure mode of straight tension specimens, with (b) the fracture surface imaged under 45° tilt. (c) Failure very close to the substrate, but within the photoresist, as common for small footprint specimens on silanized substrates. Due to high surface adhesion, residues remain on the substrate, as shown in (d) under 45° tilt, where a surface step towards the substrate indicates the remaining photoresist layer. (e) Complete detachment of the specimen from the substrate, common for untreated substrates over a large range of specimen footprints. (f) A flat surface of the substrate remains. The defined edges originate from the uniform gold coating, indicating areas formerly covered by the specimen.

substrate directly after printing in every case. The force readings during displacement-controlled loading exhibited low scattering in the range of 10 µN, and this raw data is depicted in the graphs. Two characteristic values were determined and marked in the graphs for further evaluation steps. Firstly, the yielding force f_y, defined as the force at which the force–displacement curve is intercepted by 90 % of the initial specimen stiffness. Secondly, the failure force f_f, which is the last datapoint before the force drop. The respective failure modes are indicated by the markers as described in Fig. 3. Thirdly, the total work until failure U_f is calculated from area beneath the load vs. displacement curve, as indicated in Fig. 4(b). The yield and failure stresses (derived from respective forces) were compared across various specimen areas (see Fig. 5 for yield and Fig. 6 for failure) and for the different failure modes (see Fig. 8(a)).

Comparing the silanized and untreated substrates, the former specimens show an explicit yielding section after the defined yield point is reached, regardless of size. For the latter, this section only develops at larger footprint specimens. SEM images obtained during testing confirm the specimen detachment from the unsilanized substrate (Fig. 3(e)) and show considerable plastic deformation in the highly stressed regions of the adhering specimens before failure.

In Fig. 5, individual yield stress values σ_y, are plotted against the model specimen footprint area a^2 for both substrate conditions. The yield stress σ_y is obtained by dividing the yield force f_y by the minimum yield cross section area A_y, similar to common engineering tensile stress evaluation [68]. A_y was determined for various fracture surfaces of area A_f, and averaged for each individual specimen group for failure near the surface ($A_y = f(a^2)$) and failure at the gauge section (constant A_y). A_f and A_y suffers from uncertainties regarding surface area measurements by SEM images. A maximum relative error (standard deviation) of 10 % is estimated from multiple fracture surface measurements on the smallest specimens. This value decreases with increasing surface area in the section $A_y = f(a^2)$ group until a relative error of 4 % is reached, also indicated by constant A_y. The scattering within the data is a combination of experimental errors, such as imperfect specimen alignment or finite stiffness of the setup, and uncertainties regarding A_y. For data visualization, the ideal modeled footprint area a^2 was used rather than the measured one to more clearly depict trends across the experiments.

For both substrate conditions, the force increases with minimum

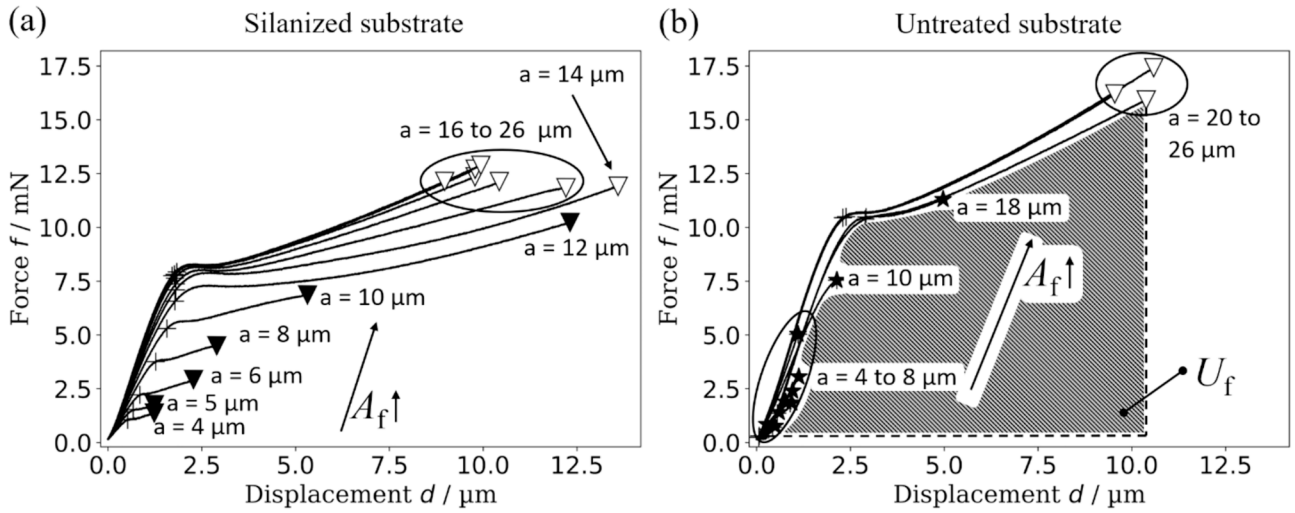

Fig. 4. Representative load vs. displacement data of specimens with increasing footprint size on (a) silanized and (b) untreated substrates. Characteristic yield (black crosses) and failure (as Fig. 3) data are marked, respectively.

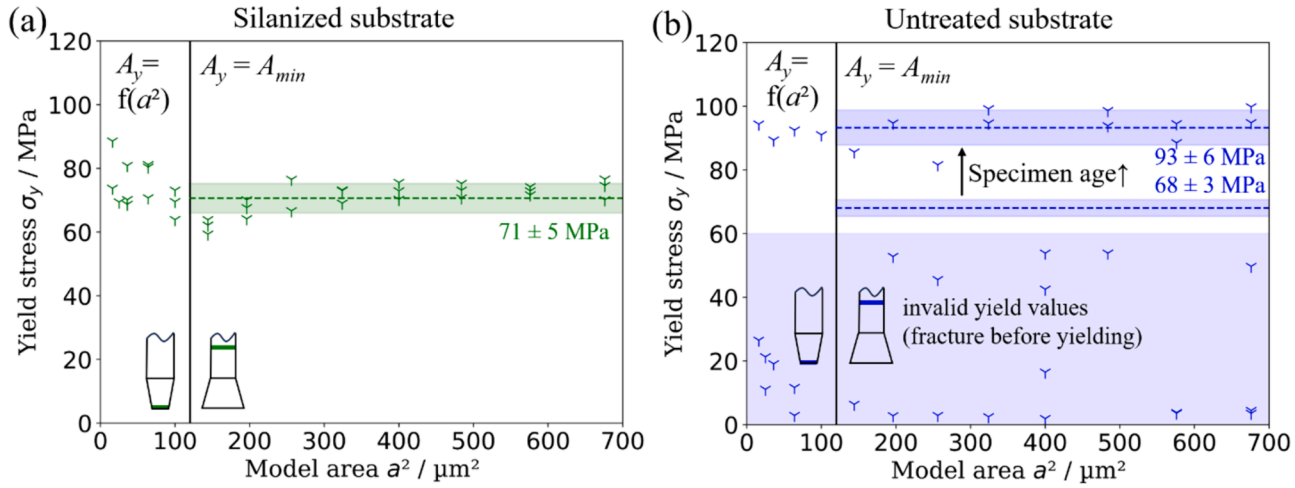

Fig. 5. Yield stress σ_y vs. model footprint size a^2 on (a) silanized and (b) untreated substrates. (a) Samples on the former exhibited considerably lower scatter and a well-defined stress plateau of 71 MPa, where the yielding is defined by the bulk material. (b) On untreated substrate, the stress did not decrease with model area, but shows a higher level (93 MPa) for aged specimen. Equally old specimens yielded comparable values on both substrates (68 MPa). Extraordinarily low yield stress values developed due to early failure through complete detachment.

specimen cross section until the failure mechanism changes from substrate-near to gauge failure. Only the latter facilitates the development of a distinct yielding plateau. On silanized substrates (see Fig. 5 (a)), σ_y shows an initial decrease followed by a well-defined plateau at 71 MPa, with 5 MPa standard deviation. The onset of the plateau is defined solely by the equality of the footprint area and the cross-sectional area of the specimen's gauge, which is reached at $a \sim 12$ µm and leads to uniform straining. Specimens on the untreated substrate (see Fig. 5(b)) show no distinct decrease of the yield stress σ_y with cross section area, but a general higher value of 93 MPa and 6 MPa standard deviation. As the yield stress should be inherent to the material, experiments on the untreated substrate were repeated. The second testing session was conducted with specimens at the same aging times as on the salinized substrate, resulting in comparable values of 68 MPa and 3 MPa standard deviation. Considerably lower yield stress values on the untreated substrate originated from artefacts due to early failure of the specimens, as no reliable yielding point can be defined before final failure.

In Fig. 6, the failure stress σ_f, obtained by dividing the failure force f_f by the individual fracture surface area A_f, is plotted over the theoretical footprint area a^2. Like Fig. 5, the different color codes of Fig. 6(a) and (b) underline the different substrate conditions. Furthermore, the failure mode is distinguished between failure at the specimen's gauge (see Fig. 3(a)), indicated by filled markers, and failure at the base, shown by empty markers (see Fig. 3(c) and (e)). As described above, the accuracy of A_f suffers from visual uncertainties on SEM images, with an error that declines from roughly 10 % to 4 % until constant A_f is reached, indicating failure within the gauge section. Potential increases in surface area due to roughness or curvature were ignored due to inaccessibility and negligible contributions. Points marked with brackets indicate increased uncertainties with regards to individual A_f values, *e.g.* preceding detachment features on the contact surface.

On the silanized substrate, the failure stress σ_f decreased slightly with model area at first, reaching a minimum of about 95 MPa, before σ_f recovering slightly. As the failure mode changed from near-surface to gauge failure, the failure stress stayed roughly constant between 100 and 130 MPa. Gauge failure at the untreated substrate developed at a slightly higher stress range than stress levels for yielding, between 120 and 160 MPa. Results from the second set of experiments with matching specimen age showed lower failure stresses, in agreement with

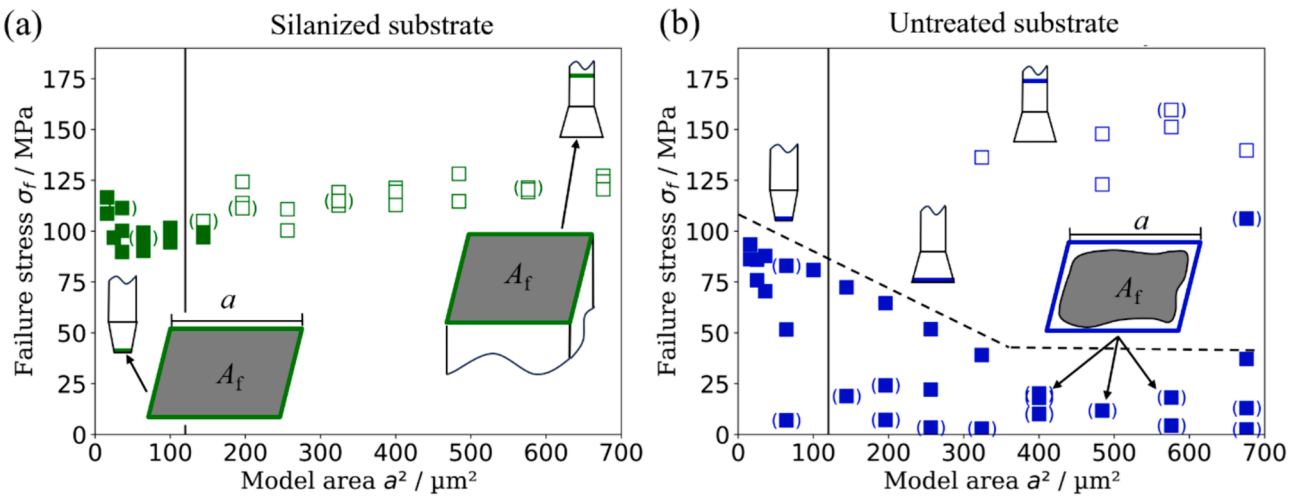

Fig. 6. Failure stress σ_f vs. nominal footprint area a^2. (a) Tensile specimens on the silanized substrate showed a slight decrease in failure stress, which recovered until the failure mechanism changed from surface-near to gauge failure, with a constant stress level. (b) Specimens on untreated substrate show considerably increased scatter and the transition of failure mode (from detachment to gauge failure) is shifted towards higher footprint area.

experiments on the silanized substrate. In general, the behavior of the untreated substrate is much more stochastic. For the detachment failure mode, a considerable decrease in failure stress is observed, as well as a shift in the approximate transition footprint to a considerably higher model area a^2. However, no precise footprint for sufficient adhesion was found, as even the largest footprints experienced detachment failure at the base. A dashed line was introduced in Fig. 6 as guide for the eye for visualization.

Data points at very low failure stresses mainly correspond to "uncertain" area measurements. In these cases, the footprint area remaining after failure did not have a defined edge, as would be expected in a sample coated uniformly in gold, but by a "washed out" shape, suggesting detachment before coating. A comparison of the sharply defined and blurred specimen footprints after testing, depicted in Fig. 7, led to the assumption that partial detachment below specimens occurred prior to application of the gold film (at or after specimen writing), with a corresponding gap confirmed by SEM images before testing.

To summarize the stress data of the distinct failure events, a cumulative distribution is plotted in Fig. 8(a), where non-valid points (marked with brackets) are neglected. In general, specimens on the silanized substrate (plotted in green) display a narrower and more defined distribution, compared to the higher scatter of the untreated substrate (shown in blue). To allow direct comparison between failure modes, median values (intersection with the 50 % line) of the stress levels are used. The failure stress for the gauge is higher for the aged set of experiments on untreated substrate, with a value of ~ 140 MPa compared to ~ 120 MPa for the specimens on the silanized substrate. The differences in failure modes (detachment and substrate-near cracking) are also well reflected in the stress distribution, with nearly no overlap in median values. The adhesion stress was 70 MPa, with a maximum value of around 90 MPa. In contrast, the substrate-near failure occurred around 100 MPa, with just a few outliers at higher and lower stresses. Based on these results, the pure adhesion strength increases by at least a factor of 1.4 for silanized substrates. However, since the specimen failed within the initial layers rather than at the exact interface between photoresist and substrate, only a lower bound can be stated with certainty.

To facilitate a comparison between work-of-adhesion/failure-based results, the specific work of failure u_f was estimated for each specimen by normalizing the total work of failure U_f with the fracture surface area A_f. A representation, analogous to the essential work of fracture (EWF) [69,70], can be constructed. There, the dissipative part of the work of fracture scales with a representative volume within the ligament and the

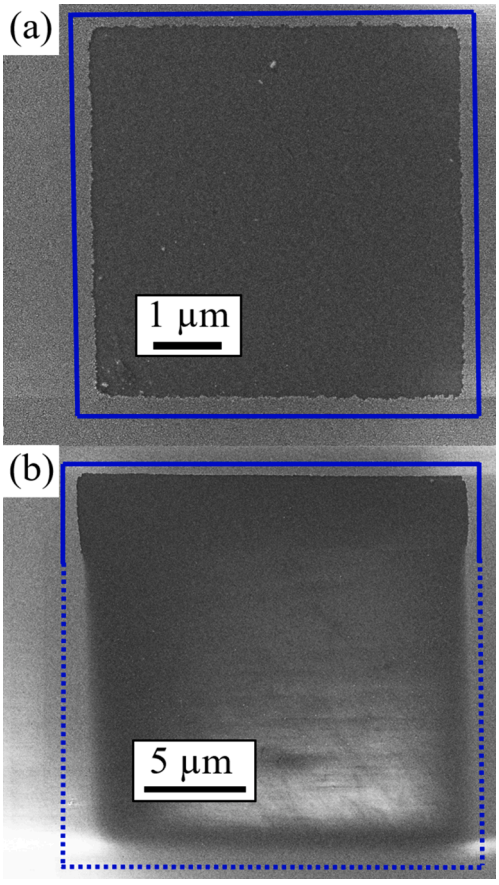

Fig. 7. Specimen footprints after detaching from an untreated substrate. (a) A uniformly adhering specimen left a sharply defined footprint within the uniform gold layer after testing. (b) The "washed out" shape is a consequence of non-uniform coverage of the substrate due to partial detachment of the structure before application of the gold layer. As a result, the specimen only leaves a shadow during sputter coating. Such footprints point to poor adhesion on the untreated substrate, which is the main reason for a pronounced uncertainty in the measurements.

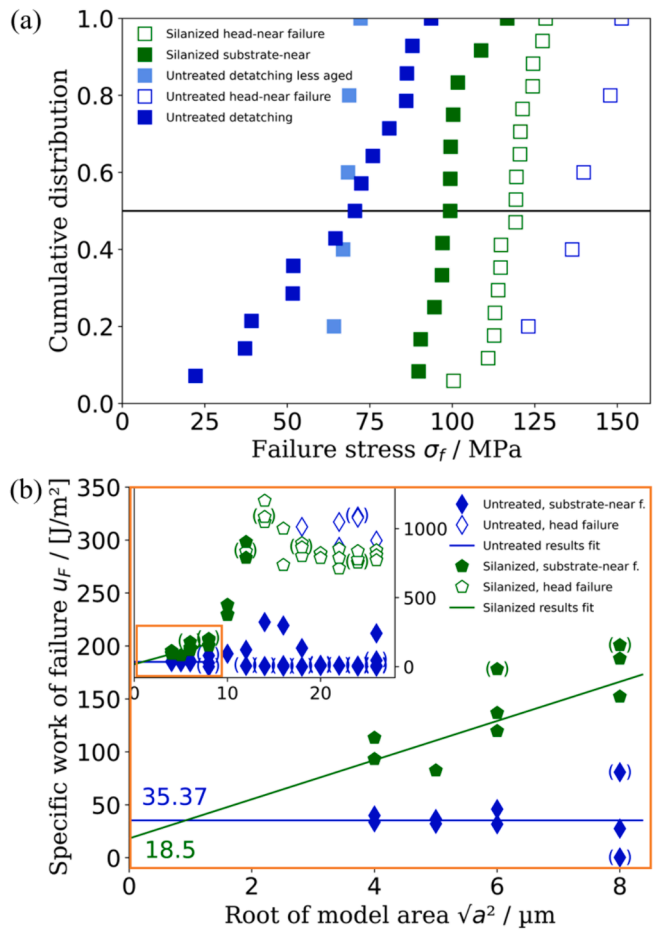

Fig. 8. (a) Cumulative distributions of failure stresses for the various failure modes, including a 50 % line to facilitate comparison of median values. Yield and failure stresses show a narrow distribution on the silanized substrate and a broader distribution on the untreated one. In the latter case, the stresses appear considerably decreased, as the specimens tended to detach at their base, which did not occur for the silanized substrates. (b) The specific work of failure, plotted over the root of the model area to facilitate a linear fit on the mechanically constrained section, is comparable to other adhesion measurement techniques.

essential part with ligament area. The plastic deformation in the present adhesion experiments is constricted to the bottom of the smaller footprint specimens, due to the locally acting higher stresses, which can only surpass the yield threshold up to a certain height above the substrate interface. By applying a normalization analysis, the deformed volume will scale with $\sim a^3$, independent of the actual shape of the plastically deforming volume, while the adhering interface scales with $\sim a^2$. This allows the separation of essential (interface inherent) adhesion work from dissipative work using a linear scaling over a for various footprint areas. In Fig. 8(b), u_f is plotted over the root of the nominal footprint area a^2, equivalent to the side length of the specimen's square base. For the silanized substrates, a linear fit is applied to the initial section, assumed to demonstrate spatially confined plasticity within the specimens. The y-intercept agrees well with a previously determined value for the EWF, which was reported to be between 7.6 and 26.3 J/m^2 [39] for the same photoresist and varying laser writing power. The case of the untreated substrate showed no linear relation, but rather a constant maximum work of detachment. An average value over all valid data points was calculated. The inset of the figure shows all results, including footprints larger than the gauge section for completeness. However, these results cannot follow the same scaling behavior, as the constriction of plastic deformation is not at the bottom, but rather at the gauge section, and are therefore considered invalid for the ongoing discussion with regards to adhesion work.

4. Discussion

The parameters applied during the slicing procedure determine the local exposure dose within an obtained body, which is inherently defined by conversion rate of the monomers, thus affecting the mechanical properties [39,71]. In a previous work, yield strength and Young's modulus were directly linked to the writing parameters, and a model for these properties, based on the degree of conversion, was presented [58,60]. Unsuitable parameters may therefore cause an inhomogeneous dose distribution, which can strongly decrease the materials performance. This parameter-dependent nature of the photopolymer, might also potentially influence the general adhesion properties [36]. Herein, the focus was laid on demonstration of the methodology, but future work in this field might select a single suitable geometry and perform parameter variation to further explore the effect of writing parameters on the adhesion. The printer system utilized in this work enabled the selection of different parameters for the initially printed layers, which might be turned based on a previous investigation into optimal adhesion. However, from a practical viewpoint, the preselected parameters for bulk printing will be used initially, and subsequently tuned as required, as it was done in the present work.

The yield and fracture force measurements for the first set of untreated substrate experiments increased by about 25 %, compared to the results of the silanized ones (compare Fig. 4(a) vs. (b) or Fig. 5(a) vs (b)). Since the same batch of photoresist and process parameters were used, specimen aging effects were investigated. The initial specimens on the untreated substrate were about 300 days old, whereas specimens on the silanized substrate were only 30 days old before testing. Consequently, a second set of specimens were manufactured on an untreated substrate. Around 80 % of these specimens did not survive the development procedure due to bad adhesion. The few remaining were tested after 30 days, and displayed "uncertain" adhesion surfaces due to partial detaching. Within Fig. 5(b), only the mean value and standard deviation of the less-aged specimens are shown, as unfortunately only the dummy specimens with an increased contact area footprint of $a^2 \sim 2500$ µm^2 could be used for yield onset calculation. All the others showed detaching failure at the substrate-specimen interface. Despite this, the yield stress agrees well with the equally aged specimens on silanized substrates (shown in Fig. 5(a)), confirming that the previously determined increased yield stresses were a result of aging. Detailed investigation of this phenomenon is outside the scope of the present manuscript and will be the focus of future work, but the identified yield stress range agrees well with stress values reported elsewhere [58,71] obtained on specimens with unspecified age. As the second set showed considerably fewer adhering specimens, the data from the first set of experiments should be considered an upper bound for adhesion.

Regarding the yield stress on the silanized substrate (see Fig. 5(a)), a small initial decrease with model area is present. This knee-like trend is not present for the specimens on the untreated substrate. Noreworthy, there is increased uncertainty in surface area (up to 10 %) for the smallest footprints. However, this may be due to the straight definition (intersection with line of 90 % initial stiffness, see Fig. 4(a)) overestimating yield forces for smaller specimens due to the non-self-similar evolution with the model area a^2. Smaller specimens in particular show a knee in the load vs. displacement behavior instead of a defined yielding plateau. Sufficient adhesion is necessary for reaching the yielding plateau (for both substrate conditions) and only specimens showing failure within the gauge section ($a > 12$ µm, with a nearly constant cross section area) will give meaningful values for the yield stress. So, the change in force vs. displacement behavior originates presumably from a geometric confinement effect.

For small footprints, a confined volume close to the substrate underwent stress and yielded prior to other regions, thus prohibiting the

development of a defined and broad yielding section. An analogy to the standard sized specimen can be drawn, where the strain until failure is a function of the specimen gauge length. If the specimen's footprint area is similar to the gauge cross-sectional area, a large volume of the specimen yields uniformly, resulting in a distinct yielding plateau. If the specimen's footprint area surpasses the gauge's cross section, only the gauge region is uniformly strained, comparable with common tension specimen geometries. This effect is highlighted by the change in failure position (corresponding to the most strained location) from near the surface towards the gauge section near the specimen's head. Like the yield stress, the failure stress (see Fig. 6(a)) also initially decreased with the model footprint area a^2 until the failure position changed from bottom to gauge at the point of uniform gauge cross section, located at modeled footprint area $a^2 \sim 144\ \mu m^2$ (with actual footprint dimensions of $10.4 \times 10.4\ \mu m^2$ and actual gauge cross section of $9.0 \times 12.0\ \mu m^2$). Due to superior adhesion of specimens, even the interface delamination is suppressed completely, as the strong adhesive anchoring moves the most critical point towards the inside of the photoresist. Thus, a layer of photoresist always remains on the substrate, proving that, in general, the adhesion is higher than the failure strength (see Fig. 4(c)).

Analogous to the yield stress, the failure stress (see Fig. 6(a)) also experiences a small initial decrease that recovers at $a^2 \sim 30\ \mu m^2$. This trend is presumably due to a confinement effect within the resin, rather than at the interface, for the silanized substrate. A straightforward stress calculation based on footprint area (as performed herein) only considers uniaxial stresses along the specimen direction. However, configurational effects due to the actual shape of the specimen near the substrate-resist interface, where different elastic properties (Modulus and Poisson's ratio) lead to perpendicular stress components and therefore an increased capability for plastic deformation before failure, due to a three-axial stress-state at the interface. As the ratio between footprint and gauge section area increases, the plastically deformed volume increases and the influence of stress-triaxiality at the interface becomes negligible in comparison to the uniform uniaxial stress field. This is likely the cause of the initial decrease in failure stress, up to an approximately constant regime for $a^2 > 30\ \mu m^2$. Finite element simulation might be suitable for studying these influences in-depth [72,73].

In strong contrast to the specimens on the silanized substrate, specimens on the untreated one detached due to inferior adhesion, including specimens with footprints considerably surpassing the specimens gauge sections area (see Fig. 6(b)). Many specimens did not survive the development procedure, and, if they did, gaps below the specimen's footprint due to bad adhesion were evident in the *in situ* SEM images, as well as the *post mortem* fracture surface investigations. As a result, a large fraction of these specimens had an extraordinarily low detaching force and "uncertain" adhesion area (as described above, see Fig. 7). Curing and shrinking stress, further worsened by occasional local pollution, is presumably the reason for this partial detachment in these cases. Nevertheless, for the cases where mechanical tests were possible, a decrease in yield strength or a minimum of failure stress (see Fig. 6(a) vs. (b)) was not evidenced on the untreated substrate specimens. Only a few valid values of yield stress (see Fig. 5) could be obtained from around double the number of specimens. There was no clear dependency with model footprint area a^2.

The trend of decreasing fracture stress (due to the actual detachment) extends to considerably higher specimen footprints on the untreated specimens (see Fig. 6(b)). Similar behavior was previously reported by Izard *et al.* [43]. There, the decrease of failure strength was less pronounced, presumably due to the shear specimen configuration. However, according to their data as well as the present experiments, the decrease in adhesion is mainly governed by defects at the interfaces acting as stress concentrators. Such crack-tip like defects mostly originate from photoresist curing and shrinkage/swelling – which lead to upwards bending deformation at the outermost borders of the specimen – as well as the removal of remaining resin during the development step [35,36]. This would explain the present trend of decreased adhesion strength with increased adhesion area, as larger areas would lead to increased bending deformation, and thus more interface detachments and higher stress concentrations at equal nominal stresses. A simple measure for counteracting the delamination tendency was reported by Lee et al [36], where a direct post-curing process at laser writing by double scanning initial layers reduced swelling and therefore delamination.

For a straightforward comparison of adhesion strengths for both substrate conditions, Fig. 8(a) depicts a cumulative distribution of the stress values for the respective failure case, as plotted in Fig. 6, assuming a normal distribution for simplification. The difference between gauge failure data, which would be expected to show equal failure stress due to identical failure mechanisms despite the different substrate conditions, is explained by the different specimen age (see Fig. 5(b) for the difference in yield stress). One specimen of the second prepared set failed within the gauge section at 119 MPa, though this was not included in the plot due to lack of repeatability. Although only a single data point, it supports the assumption of age dependence, as it fully resides within the failure stress distribution of the salinized substrate specimens. Consequently, the failure stress was around 120 MPa for the 30 day old resin, and around 140 MPa for the roughly 300 day old resin. The agreement of detachment stress at approximately 70 MPa between the two sets of experiments on untreated substrates (brighter and darker blue squares) confirms the independence of adhesion characteristics with respect to specimen age. However, the failure near the silanized substrate interface at approximately 95 MPa shows nearly no overlap with both the untreated datasets, highlighting the difference in failure mode. The quantified value can be used as a reliable lower bound measure of adhesion on a small scale, proving the effectiveness of silanization for the given substrate/resin combination.

However, due to the remaining resin on the substrate, this value represents a material property, rather than an interface adhesion-specific parameter. To find this parameter, a different approach based on energy considerations can be attempted. Since the material fails in the constraint region, the final mode can be considered a combination of the material's intrinsic mechanical properties and the geometrical confinement near the substrate. The principal material failure under plane stress conditions within a confined volume is commonly described by an EWF approach, which was originally developed for fracture testing of thin metal sheets [69,70,74], but is nowadays extensively applied on polymeric films [75]. This principal was later transferred to polymer–polymer interfaces as well [76]. Although it is a fracture mechanical approach, relying on the presence of a sharp crack, the fundamental idea is that the work for interface adhesion scales with area ($\sim a^2$), while the work dissipated by plastic deformation scales with volume ($\sim a^3$). This can be transferred to the present case, where a constrained uniform stress distribution is present within the very first few layers of the polymer near the substrate, and therefore the volume/area scaling should be applicable. The standardized EWF evaluation requires a normalization of the total work of fracture within the specimens' cross section, which is plotted over the ligament length to as measure the outer fracture process zone. The ligament length is replaced by the square root of the specimen's footprint area, as plotted in Fig. 8(b). The EWF is not related to the size of surrounding process zone, and therefore obtained from the y-intercept along the described linear plot. The work related to the process zone is given by the slope of the linear fit, which also includes a geometry parameter to relate the ligament length to the surrounding volume. The following discussion should be considered an estimation of the EWF rather than a detailed analysis of the related fracture process zones, due to the aforementioned simplifications and assumptions. For a straightforward analysis of the essential work, the linearity, collapsing around at an $\sqrt{a^2}$ of 10 μm, is considered specific enough to apply the fundamental EWF concept (see Fig. 8(b)). Using this method, an EWF of around 19 J/m^2 was found, in agreement with data on the same material (9 – 26 J/m^2), albeit processed with slightly larger laser powers [39]. This agreement is quite favorable when considering

the simplifications and differences in geometry.

Equivalent analysis cannot be applied to the untreated substrate experiments, as it has a stochastic, but quasi-constant specific work of failure for all footprint sizes. Therefore, only a mean value is presented in the plot of Fig. 8(b). The actual interface failure gives a size independent value of around 35 J/m^2, which is higher than the deduced essential fracture work of 19 J/m^2 of the photoresist. If true, these results would indicate that less energy is required to fracture of the photoresist than to detach a specimen with a footprint size below the intersection point of the green (EWF) and blue (dethatching energy) trend line. The presented method is unsuitable for small specimens above the trend line, as specimens with an a of 2 μm collapsed in every trial, requiring a different approach outside the scope of this publication. It is important to emphasize the different failure principles between the two scenarios, and that, to explain the intersection point, extrapolation may also suffer from scatter within the experimental data. Despite this, the acquired data underlines a the considerable increase of adhesion strength, as, in all cases, the silanized substrates had a higher experimental work until failure for equally sized specimens, proving practical relevance.

Finally, the detaching failure mode, associated with interface failure, can be put into a larger context, involving at least one interface energy consideration. All common failure models for adhesion/separation are based on the materials' surface energies, which are by themselves diversely characterized and can be combined to find the interfacial energy contribution [77]. A detailed discussion on the chemical nature of the interface itself will not be offered, but it is possible to rationalize the presented results from an experimental perspective. To open the interface between the photoresist and the fused silica substrate, a certain amount of energy has to be spent (by an external load), which, at minimum, must be in the range of the surface energies of both newly exposed surfaces, minus the actual interaction term [78]. At maximum, this simple summation of surface energies (determined via the Owens-Wendt method) would yield 86.5 mJ/m^2 (neglecting interaction terms). Hence, this simple thermodynamic approximation is roughly 400 times smaller than the measured value of 35 J/m^2 for specimen detaching from the substrate. Therefore, additional dissipative mechanisms, not considered by purely thermodynamically based surface-energies-based models [79], greatly affect the adhesion. The highest energy will be near interface plastic deformation, although stochastic bond formation (covalent, H-bond, ect.) might occur, as well as viscoelastic flow phenomena [80]. Furthermore, chemical parameters, such as local mean molecular weight and distribution [81], might be involved, which are generally challenging to analyze. It is essential to determine such adhesion parameters in a direct experimental manner, as demonstrated herein, and not rely solely on indirect global parameters such as surface energies.

Finally, to highlight the general applicability of our novel approach, a demonstration of local printing capabilities of the presented specimen geometries is offered, in order to encourage further work on localized adhesion testing for devices with various materials exposed on the surface. Fig. 9 depicts surface adhesion tension specimens on various parts of a polished electronic integrated circuit (IC), including peripheral surface mounted device (SMD) components sitting together on a single printed circuit board (PCB). This PCB was taken from electronic scrap, cut down in dimensions to the section shown in Fig. 9(a), fitted within the MPL device, and polished to about half the thickness of the IC chip to expose inner components. Selected specimens were processed as described above, including the gold coating for SEM imaging. Fig. 9(b) depicts a zoomed SEM image section of two SMD components, upon which specimens were manufactured. Subsets are depicted in Fig. 9(c), (d), where individual specimens are located on the metalized zones, solder or ceramic materials respectively, of the SMD devices. Positioning in terms of plane direction is accurate to a few μm, whereas the onset of printing must be defined manually by sharpness impression and iterative printing attempts. In Fig. 9(e), another location, directly on the opened IC, is depicted. Here, additional specimens were manufactured and marked sitting on different material surfaces. Fig. 9(f) depicts a specimen in a region that appears to be the heat sink metallization, beneath an IC and close to the embedding polymer. Finally, Fig. 9(g) and (f)

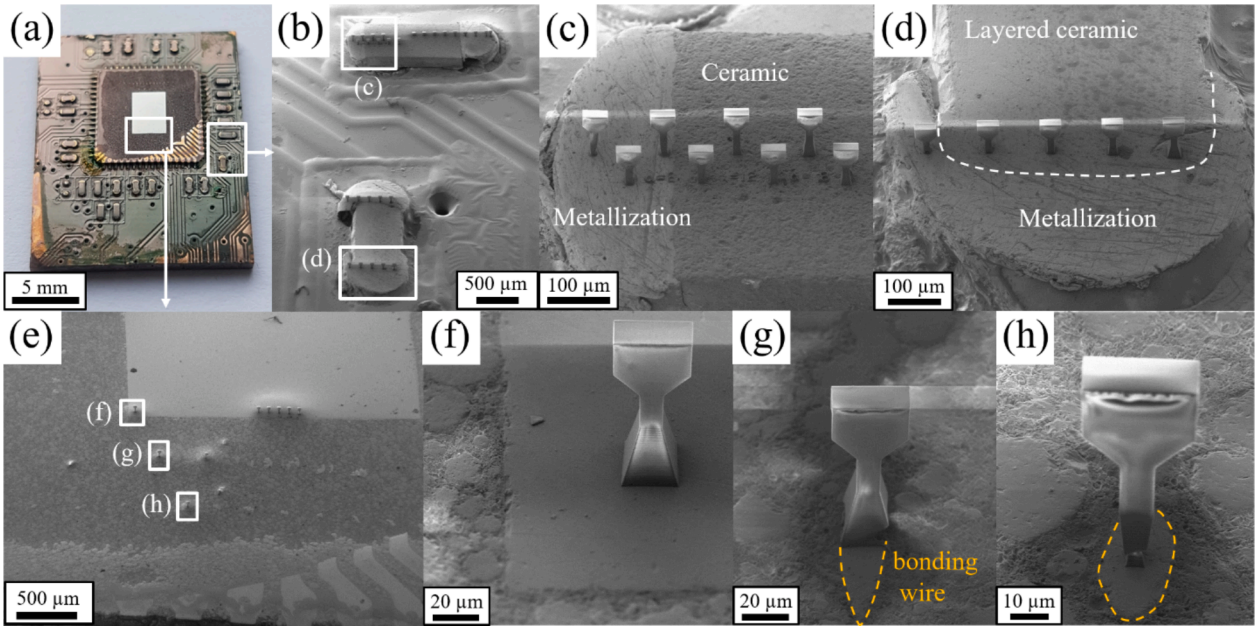

Fig. 9. Printed adhesion tension specimen on target positions of a non-specified polished IC chip and surrounding SMD components. (a) Overview, showing the entire PCB (green) with soldered on components, which were grinded to about half original height and used as printing substrate for demonstration reasons. (b) Magnified section on two different polished SMD components bearing multiple specimens each. (c) Two rows of specimens with various footprint areas, with three located on a metalized part of the SMD and the remaining specimens on the ceramic part. (d) Various adhesion specimens close to the ceramic/solder-interface of a on a differently orientated SMD than in (c). (e) Zoomed-in section of a different part of the polished chip, selected as printing position. (f) Individual specimens on the heat sink metallization of the IC. (g),(h) Adhesion specimens printed to cross-sections of bonding wires with ~ 20 μm diameter, for demonstration of targeted specimen printing.

depict two specimens with different footprints, located directly on the cross sections of bonding wires with a diameter of ~ 20 μm, used for contacting ICs from the top. The center of the bonding wire center was reached with great precision, proving the applicability for small scale surface features.

The presented example showcases the possibilities of the methods presented in this paper. Future works might facilitate surface adhesion testing on semiconductor materials, such as silicon or gallium arsenide, to prove the general applicability of the method for technologies like photonic circuits. When considering the chemical characteristics of a silicon surface, which commonly contains a natural oxide, the silanization treatment should be comparably effective as on silica [42,82–84]. In that specific case, the reflectivity of the surface must be considered, which will increase the dose on initially printed layers, over the proper proportions, and therefore cause degradation. Such defects are visible towards the base of the printed specimens on a metal surface, shown in Fig. 9(g) and (f), but can be avoided with selection of adapted laser writing parameters.

5. Conclusion

Various potential application fields will continue to benefit from and rely on the specific chemistry of the substrate or photoresist surfaces, and therefore, modification–related topics will gain increasing importance. In the present work, a methodology for quantitatively accessing the adhesion strength on a very localized scale was successfully implemented, which can be straightforwardly applied to any arbitrary MPL-resist-substrate pairing and using tension specimens with a tuned geometry for varying adhesion surface. Complementary SEM image information, as well as a nearly ideal introduction of uniaxial tensile stress are key features of the presented methodology, in strong contrast to common shear mode testing. A quantitative assessment of adhesion strength in pure tension, directly on the photoresist–substrate interface, was performed for the first time, using tension specimens with a tuned geometry to test varying adhesion surfaces. For a demonstration of the method on a pretreated surface, wet silanization as a common and easily applicable pre-treatment for MPL-printing substrates was investigated. The adhesion stress requirement for specimen detachment on an untreated substrate was determined to be around 70 MPa, displaying highly stochastic behavior and a strong trend towards decreasing adhesion strength with model area. For silanized substrates, failure within the material, rather than full detachment, is observed, suggesting that the adhesion surpasses the materials strength. The photoresist used had an adhesion strength of around 95 MPa, which may be considered as a safe upper threshold for adhesion on silanized substrates if minor dependency with model area is neglected. However, this value represents a mixture of the polymer's cohesion and geometric effect of the chosen specimen geometry. In future works, further equivalent tension specimens could be manufactured on target positions of pre-treated fiber glass or semiconductor substrates to quantitatively investigate adhesion properties. In particular, catheter-like fiber optical lens stacks, like those used in sensors, which are exposed to surrounding liquid movement or photonic coupler plugs, would benefit from adhesion durability assessments. Alternatively, thin film delamination behavior of coating systems could be investigated, if superior adhesion to the most superficial layer is guaranteed, simliar to a miniaturized tape test.

CRediT authorship contribution statement

Alexander Jelinek: Writing – original draft, Visualization, Methodology, Investigation, Formal analysis, Conceptualization. **Elisabeth Rossegger:** Writing – review & editing, Investigation. **Sandra Schlögl:** Writing – review & editing, Resources. **Daniel Kiener:** Writing – review & editing, Supervision, Resources, Funding acquisition. **Markus Alfreider:** Writing – review & editing, Investigation, Formal analysis.

Declaration of competing interest

The authors declare that they have no known competing financial interests or personal relationships that could have appeared to influence the work reported in this paper.

Data availability

Data will be made available on request.

Acknowledgements

The infrastructure was funded by the Austrian Research Promotion Agency (FFG) in the framework of the F&E infrastructure program SmartNanoTop (ffg.at) [grant number 870449], which is thankfully acknowledged. The authors acknowledge funding by the European Research Council [grant number 771146] (DK). The authors would like to thank Tess Obuchowski for proofreading and formal language corrections.

References

[1] X. Zhou, Y. Hou, J. Lin, A review on the processing accuracy of two-photon polymerization, AIP Adv. 5 (2015) 030701, https://doi.org/10.1063/1.4916886.
[2] J. Fischer, M. Wegener, Three-dimensional optical laser lithography beyond the diffraction limit: 3D optical lithography off limits, Laser Photonics Rev. 7 (2013) 22–44, https://doi.org/10.1002/lpor.201100046.
[3] L. Guan, C. Cao, X. Liu, Q. Liu, Y. Qiu, X. Wang, Z. Yang, H. Lai, Q. Sun, C. Ding, D. Zhu, C. Kuang, X. Liu, Light and matter co-confined multi-photon lithography, Nat. Commun. 15 (2024) 2387, https://doi.org/10.1038/s41467-024-46743-5.
[4] J.K. Hohmann, M. Renner, E.H. Waller, G. von Freymann, Three-dimensional μ-printing: an enabling technology, Adv. Optical Mater. 3 (2015) 1488–1507, https://doi.org/10.1002/adom.201500328.
[5] V. Harinarayana, Y.C. Shin, Two-photon lithography for three-dimensional fabrication in micro/nanoscale regime: A comprehensive review, Opt. Laser Technol. 142 (2021) 107180, https://doi.org/10.1016/j.optlastec.2021.107180.
[6] H. Wang, W. Zhang, D. Ladika, H. Yu, D. Gailevičius, H. Wang, C. Pan, P.N.S. Nair, Y. Ke, T. Mori, J.Y.E. Chan, Q. Ruan, M. Farsari, M. Malinauskas, S. Juodkazis, M. Gu, J.K.W. Yang, Two-photon polymerization lithography for optics and photonics: fundamentals, materials, technologies, and applications, Adv. Funct. Mater. 33 (2023) 2214211, https://doi.org/10.1002/adfm.202214211.
[7] A. Jaiswal, C.K. Rastogi, S. Rani, G.P. Singh, S. Saxena, S. Shukla, Two decades of two-photon lithography: Materials science perspective for additive manufacturing of 2D/3D nano-microstructures, iScience 26 (2023), https://doi.org/10.1016/j.isci.2023.106374.
[8] J. Linkhorst, J. Lölsberg, S. Thill, J. Lohaus, A. Lüken, G. Naegele, M. Wessling, Templating the morphology of soft microgel assemblies using a nanolithographic 3D-printed membrane, Sci. Rep. 11 (2021) 812, https://doi.org/10.1038/s41598-020-80324-y.
[9] M. Oellers, F. Lucklum, M.J. Vellekoop, On-chip mixing of liquids with swap structures written by two-photon polymerization, Microfluid. Nanofluid. 24 (2020) 4, https://doi.org/10.1007/s10404-019-2309-8.
[10] R.K. Jayne, M.Ç. Karakan, K. Zhang, N. Pierce, C. Michas, D.J. Bishop, C.S. Chen, K. L. Ekinci, A.E. White, Direct laser writing for cardiac tissue engineering: a microfluidic heart on a chip with integrated transducers, Lab Chip 21 (2021) 1724–1737, https://doi.org/10.1039/D0LC01078B.
[11] C. Michas, M.Ç. Karakan, P. Nautiyal, J.G. Seidman, C.E. Seidman, A. Agarwal, K. Ekinci, J. Eyckmans, A.E. White, C.S. Chen, Engineering a living cardiac pump on a chip using high-precision fabrication, Sci. Adv. 8 (2022) eabm3791, https://doi.org/10.1126/sciadv.abm3791.
[12] C. Flynn, H. Cao, B.E. Applegate, T.S. Tkaczyk, Fabrication of waveguide directional couplers using 2-photon lithography, Opt. Express 31 (2023) 26323, https://doi.org/10.1364/OE.495363.
[13] W. Hartmann, P. Varytis, H. Gehring, N. Walter, F. Beutel, K. Busch, W. Pernice, Waveguide-Integrated Broadband Spectrometer Based on Tailored Disorder, Adv. Optical Mater. 8 (2020) 1901602, https://doi.org/10.1002/adom.201901602.
[14] G.O. Dias, O. Lecarme, J. Cordeiro, E. Picard, D. Peyrade, Microscale white light emitters fabricated by two-photon polymerization lithography on functional resist, Microelectron. Eng. 257 (2022) 111751, https://doi.org/10.1016/j.mee.2022.111751.
[15] F. Beutel, H. Gehring, M.A. Wolff, C. Schuck, W. Pernice, Detector-integrated on-chip QKD receiver for GHz clock rates, npj Quantum Inf. 7 (2021) 40, https://doi.org/10.1038/s41534-021-00373-7.
[16] M. Blaicher, M.R. Billah, J. Kemal, T. Hoose, P. Marin-Palomo, A. Hofmann, Y. Kutuvantavida, C. Kieninger, P.-I. Dietrich, M. Lauermann, S. Wolf, U. Troppenz, M. Moehrle, F. Merget, S. Skacel, J. Witzens, S. Randel, W. Freude, C. Koos, Hybrid multi-chip assembly of optical communication engines by in situ 3D nano-lithography, Light Sci. Appl. 9 (2020) 71, https://doi.org/10.1038/s41377-020-0272-5.

[17] K. Vanmol, K. Saurav, V. Panapakkam, H. Thienpont, N. Vermeulen, J. Watte, J. Van Erps, Mode-field Matching Down-Tapers on Single-Mode Optical Fibers for Edge Coupling Towards Generic Photonic Integrated Circuit Platforms, J. Light. Technol. 38 (2020) 4834–4842, https://doi.org/10.1109/JLT.2020.2997090.

[18] K. Vanmol, T. Baghdasaryan, N. Vermeulen, K. Saurav, J. Watté, H. Thienpont, J. Van Erps, 3D direct laser writing of microstructured optical fiber tapers on single-mode fibers for mode-field conversion, Opt. Express 28 (2020) 36147, https://doi.org/10.1364/OE.409148.

[19] M.A. Wolff, F. Beutel, J. Schütte, H. Gehring, M. Häußler, W. Pernice, C. Schuck, Broadband waveguide-integrated superconducting single-photon detectors with high system detection efficiency, Appl. Phys. Lett. 118 (2021) 154004, https://doi.org/10.1063/5.0046057.

[20] A. Asadollahbaik, S. Thiele, K. Weber, A. Kumar, J. Drozella, F. Sterl, A. M. Herkommer, H. Giessen, J. Fick, Highly Efficient Dual-Fiber Optical Trapping with 3D Printed Diffractive Fresnel Lenses, ACS Photonics 7 (2020) 88–97, https://doi.org/10.1021/acsphotonics.9b01024.

[21] F. Glöckler, F. Hausladen, I. Alekseenko, A. Gröger, G. Pedrini, D. Claus, Two-photon-polymerization enabled and enhanced multi-channel fibre switch, Eng. Res. Express 3 (2021) 045016, https://doi.org/10.1088/2631-8695/ac34c5.

[22] J. Li, S. Thiele, B.C. Quirk, R.W. Kirk, J.W. Verjans, E. Akers, C.A. Bursill, S. J. Nicholls, A.M. Herkommer, H. Giessen, R.A. McLaughlin, Ultrathin monolithic 3D printed optical coherence tomography endoscopy for preclinical and clinical use, Light Sci. Appl. 9 (2020) 124, https://doi.org/10.1038/s41377-020-00365-w.

[23] M. Plidschun, H. Ren, J. Kim, R. Förster, S.A. Maier, M.A. Schmidt, Ultrahigh numerical aperture meta-fibre for flexible optical trapping, Light Sci. Appl. 10 (2021) 57, https://doi.org/10.1038/s41377-021-00491-z.

[24] P.N. Manghnani, V. Di Francesco, C. Panella La Capria, M. Schlich, M.E. Miali, T. L. Moore, A. Zunino, M. Duocastella, P. Decuzzi, Preparation of anisotropic multiscale micro-hydrogels via two-photon continuous flow lithography, J. Colloid Interface Sci. 608 (2022) 622–633, https://doi.org/10.1016/j.jcis.2021.09.094.

[25] L. Brigo, J.E.M. Schmidt, A. Gandin, N. Michieli, P. Colombo, G. Brusatin, 3D nanofabrication of SiOC ceramic structures, Adv. Sci. 5 (2018) 1800937, https://doi.org/10.1002/advs.201800937.

[26] E.S. Farrell, N. Ganonyan, I. Cooperstein, M.Y. Moshkovitz, Y. Amouyal, D. Avnir, S. Magdassi, 3D-printing of ceramic aerogels by spatial photopolymerization, Appl. Mater. Today 24 (2021) 101083, https://doi.org/10.1016/j.apmt.2021.101083.

[27] K. Gyak, S. Jeon, L. Ha, S. Kim, J. Kim, K. Lee, H. Choi, D. Kim, Magnetically actuated SiCN-based ceramic microrobot for guided cell delivery, Adv. Healthc. Mater. 8 (2019) 1900739, https://doi.org/10.1002/adhm.201900739.

[28] G. Konstantinou, E. Kakkava, L. Hagelüken, P.V. Warriam Sasikumar, J. Wang, M. G. Makowska, G. Blugan, N. Nianias, F. Marone, H. Van Swygenhoven, J. Brugger, D. Psaltis, C. Moser, Additive micro-manufacturing of crack-free PDCs by two-photon polymerization of a single, low-shrinkage preceramic resin, Addit. Manuf. 35 (2020) 101343, https://doi.org/10.1016/j.addma.2020.101343.

[29] R. Bernasconi, G. Prioglio, M.C. Angeli, C.C.J. Alcantara, S. Sevim, S. Pané, P. Vena, L. Magagnin, Wet metallization of 3D printed microarchitectures: Application to the manufacturing of bioinspired microswimmers, J. Manuf. Process. 78 (2022) 11–21, https://doi.org/10.1016/j.jmapro.2022.03.057.

[30] A. Aksit, S. Rastogi, M.L. Nadal, A.M. Parker, A.K. Lalwani, A.C. West, J.W. Kysar, Drug delivery device for the inner ear: ultra-sharp fully metallic microneedles, Drug. Deliv. and Transl. Res. 11 (2021) 214–226, https://doi.org/10.1007/s13346-020-00782-9.

[31] M.A. Saccone, R.A. Gallivan, K. Narita, D.W. Yee, J.R. Greer, Additive manufacturing of micro-architected metals via hydrogel infusion, Nature 612 (2022) 685–690, https://doi.org/10.1038/s41586-022-05433-2.

[32] D.W. Yee, M.L. Lifson, B.W. Edwards, J.R. Greer, Additive Manufacturing of 3D-Architected Multifunctional Metal Oxides, Adv. Mater. 31 (2019) 1901345, https://doi.org/10.1002/adma.201901345.

[33] J. Bauer, M. Sala-Casanovas, M. Amiri, L. Valdevit, Nanoarchitected metal/ceramic interpenetrating phase composites, Sci. Adv. 8 (2022) eabo3080, https://doi.org/10.1126/sciadv.abo3080.

[34] F. Kotz, A.S. Quick, P. Risch, T. Martin, T. Hoose, M. Thiel, D. Helmer, B.E. Rapp, Two-Photon Polymerization of Nanocomposites for the Fabrication of Transparent Fused Silica Glass Microstructures, Adv. Mater. 33 (2021) 2006341, https://doi.org/10.1002/adma.202006341.

[35] C.L. Davidson, A.J. Feilzer, Polymerization shrinkage and polymerization shrinkage stress in polymer-based restoratives, J. Dent. 25 (1997) 435–440, https://doi.org/10.1016/S0300-5712(96)00063-2.

[36] J. Lee, S.J. Park, S.C. Han, P. Prabhakaran, C.W. Ha, Enhanced mechanical property through high-yield fabrication process with double laser scanning method in two-photon lithography, Mater. Des. 235 (2023) 112389, https://doi.org/10.1016/j.matdes.2023.112389.

[37] A. Jelinek, S. Zak, M. Alfreider, D. Kiener, High-Throughput Micromechanical Testing Enabled by Optimized Direct Laser Writing, Adv. Eng. Mater. 25 (2023) 2200288, https://doi.org/10.1002/adem.202200288.

[38] A.A. Bauhofer, S. Krödel, J. Rys, O.R. Bilal, A. Constantinescu, C. Daraio, Harnessing Photochemical Shrinkage in Direct Laser Writing for Shape Morphing of Polymer Sheets, Adv. Mater. 29 (2017) 1703024, https://doi.org/10.1002/adma.201703024.

[39] A. Jelinek, S. Zak, M.J. Cordill, D. Kiener, M. Alfreider, Nanoscale printed tunable specimen geometry enables high-throughput miniaturized fracture testing, Mater. Des. 234 (2023) 112329, https://doi.org/10.1016/j.matdes.2023.112329.

[40] J.F. Keckes, A. Jelinek, D. Kiener, M. Alfreider, Neural Network Supported Microscale In Situ Deformation Tracking: A Comparative Study of Testing Geometries, JOM 76 (2024) 2336–2351, https://doi.org/10.1007/s11837-024-06437-1.

[41] T.-T. Chung, Y.-H. Hsu, A.-B. Wang, C.-S. Cheong, S. Shivani, C.-J. Lee, Manufacturing of substrates with different surface roughness for cell migration test by two-photon polymerization method, Procedia CIRP 71 (2018) 305–308, https://doi.org/10.1016/j.procir.2018.05.025.

[42] V.P. Schnee, N. Henry, Q. Huynh, Anti-reflective coating by 3D PDMS stamping using two-photon lithography master, Opt. Mater. 111 (2021) 110715, https://doi.org/10.1016/j.optmat.2020.110715.

[43] A.G. Izard, E.P. Garcia, M. Dixon, E.O. Potma, T. Baldacchini, L. Valdevit, Enhanced adhesion in two-photon polymerization direct laser writing, AIP Adv. 10 (2020) 045217, https://doi.org/10.1063/5.0005548.

[44] J.G. Steck, M. Afshar-Mohajer, Q. Sun, X. Meng, M. Zou, Fabrication and tribological characterization of deformation-resistant nano-textured surfaces produced by two-photon lithography and atomic layer deposition, Tribol. Int. 132 (2019) 75–84, https://doi.org/10.1016/j.triboint.2018.12.012.

[45] J.F. Busche, G. Starke, S. Knickmeier, A. Dietzel, Controllable dry adhesion based on two-photon polymerization and replication molding for space debris removal, Micro and Nano Eng. 7 (2020) 100052, https://doi.org/10.1016/j.mne.2020.100052.

[46] S.C.L. Fischer, K. Groß, O. Torrents Abad, M.M. Becker, E. Park, R. Hensel, E. Arzt, Funnel-Shaped Microstructures for Strong Reversible Adhesion, Adv. Mater. Interfaces 4 (2017) 1700292, https://doi.org/10.1002/admi.201700292.

[47] G. Meloni, O. Tricinci, A. Degl'Innocenti, B. Mazzolai, A protein-coated micro-sucker patch inspired by octopus for adhesion in wet conditions, Sci. Rep. 10 (2020) 15480, https://doi.org/10.1038/s41598-020-72493-7.

[48] Y. Wang, R. Hensel, Bioinspired Underwater Adhesion to Rough Substrates by Cavity Collapse of Cupped Microstructures, 2101787, Adv. Funct. Mater. 31 (2021), https://doi.org/10.1002/adfm.202101787.

[49] X. Zhang, Y. Wang, R. Hensel, E. Arzt, A Design Strategy for Mushroom-Shaped Microfibrils With Optimized Dry Adhesion: Experiments and Finite Element Analyses, J. Appl. Mech. 88 (2021) 031015, https://doi.org/10.1115/1.4049183.

[50] C. Delaney, N. Geoghegan, H. Ibrahim, M. O'Loughlin, B.J. Rodriguez, L. Florea, S. M. Kelleher, Direct Laser Writing to Generate Molds for Polymer Nanopillar Replication, ACS Appl. Polym. Mater. 2 (2020) 3632–3641, https://doi.org/10.1021/acsapm.0c00626.

[51] X.W. Gu, J.R. Greer, Ultra-strong architected Cu meso-lattices, Extreme Mech, Lett. 2 (2015) 7–14, https://doi.org/10.1016/j.eml.2015.01.006.

[52] B.J. Larson, J.M. Helgren, S.O. Manolache, A.Y. Lau, M.G. Lagally, F.S. Denes, Cold-plasma modification of oxide surfaces for covalent biomolecule attachment, Biosens. Bioelectron. 21 (2005) 796–801, https://doi.org/10.1016/j.bios.2005.02.005.

[53] T. Yamamoto, M. Okubo, N. Imai, Y. Mori, Improvement on Hydrophilic and Hydrophobic Properties of Glass Surface Treated by Nonthermal Plasma Induced by Silent Corona Discharge, Plasma Chem. Plasma Process. 24 (2004) 1–12, https://doi.org/10.1023/B:PCPP.0000004878.61688.4d.

[54] C. Bandl, N. Krempl, G. Berger-Weber, W. Kern, W. Friesenbichler, Application of organosilane coatings for improved anti-adhesive properties enabling facilitated demolding in polymer processing, J. Appl. Polym. Sci. 138 (2021) 50714, https://doi.org/10.1002/app.50714.

[55] A.-I. Bunea, N. Del Castillo Iniesta, A. Droumpali, A.E. Wetzel, E. Engay, R. Taboryski, Micro 3D Printing by Two-Photon Polymerization: Configurations and Parameters for the Nanoscribe System, Micro 1 (2021) 164–180, https://doi.org/10.3390/micro1020013.

[56] Y. Wang, V. Kang, E. Arzt, W. Federle, R. Hensel, Strong Wet and Dry Adhesion by Cupped Microstructures, ACS Appl. Mater. Interfaces 11 (2019) 26483–26490, https://doi.org/10.1021/acsami.9b07969.

[57] J. Zhang, H. Ding, X. Liu, H. Gu, M. Wei, X. Li, S. Liu, S. Li, X. Du, Z. Gu, Facile Surface Functionalization Strategy for Two-Photon Lithography Microstructures, Small 17 (2021) 2101048, https://doi.org/10.1002/smll.202101048.

[58] M. Diamantopoulou, N. Karathanasopoulos, D. Mohr, Stress-strain response of polymers made through two-photon lithography: Micro-scale experiments and neural network modeling, Addit. Manuf. 47 (2021) 102266, https://doi.org/10.1016/j.addma.2021.102266.

[59] J. Bauer, A. Guell Izard, Y. Zhang, T. Baldacchini, L. Valdevit, Programmable Mechanical Properties of Two-Photon Polymerized Materials: From Nanowires to Bulk, Adv Materials Technologies 4 (2019) 1900146, https://doi.org/10.1002/admt.201900146.

[60] J. Bauer, A. Guell Izard, Y. Zhang, T. Baldacchini, L. Valdevit, Programmable Mechanical Properties of Two-Photon Polymerized Materials: From Nanowires to Bulk, Adv. Mater. Technol. 4 (2019) 1900146, https://doi.org/10.1002/admt.201900146.

[61] W.P. Vellinga, R. Timmerman, R. Van Tijum, J.T.M. De Hosson, *In situ* observations of crack propagation mechanisms along interfaces between confined polymer layers and glass, Appl. Phys. Lett. 88 (2006) 061912, https://doi.org/10.1063/1.2172713.

[62] D.K. Owens, R.C. Wendt, Estimation of the surface free energy of polymers, J. Appl. Polym. Sci. 13 (1969) 1741–1747, https://doi.org/10.1002/app.1969.070130815.

[63] D. Kiener, W. Grosinger, G. Dehm, R. Pippan, A further step towards an understanding of size-dependent crystal plasticity: In situ tension experiments of miniaturized single-crystal copper samples, Acta Mater. 56 (2008) 580–592, https://doi.org/10.1016/j.actamat.2007.10.015.

[64] M. Alfreider, M. Meindlhumer, V. Maier-Kiener, A. Hohenwarter, D. Kiener, Extracting information from noisy data: strain mapping during dynamic in situ SEM experiments, J. Mater. Res. 36 (2021) 2291–2304, https://doi.org/10.1557/s43578-020-00041-0.

[65] J. Cognard, Adhesion to gold: A review, Gold Bull. 17 (1984) 131–139, https://doi.org/10.1007/BF03214677.

[66] D.A. Lamprou, J.R. Smith, T.G. Nevell, E. Barbu, C. Stone, C.R. Willis, J. Tsibouklis, A comparative study of surface energy data from atomic force microscopy and from contact angle goniometry, Appl. Surf. Sci. 256 (2010) 5082–5087, https://doi.org/10.1016/j.apsusc.2010.03.064.
[67] M.R. Khosravani, P. Soltani, T. Reinicke, Fracture and structural performance of adhesively bonded 3D-printed PETG single lap joints under different printing parameters, Theor. Appl. Fract. Mech. 116 (2021) 103087, https://doi.org/10.1016/j.tafmec.2021.103087.
[68] J.M. Gere, Mechanics of materials, 6th ed, Brooks/Cole-Thomas Learning, Belmont, CA, 2004.
[69] K.B. Broberg, Critical review of some theories in fracture mechanics, Int. J. Fract. 4 (1968) 11–19, https://doi.org/10.1007/BF00189139.
[70] B. Cotterell, J.K. Reddel, The essential work of plane stress ductile fracture, Int. J. Fract. 13 (1977), https://doi.org/10.1007/BF00040143.
[71] N. Rohbeck, R. Ramachandramoorthy, D. Casari, P. Schürch, T.E.J. Edwards, L. Schilinsky, L. Philippe, J. Schwiedrzik, J. Michler, Effect of high strain rates and temperature on the micromechanical properties of 3D-printed polymer structures made by two-photon lithography, Mater. Des. 195 (2020) 108977, https://doi.org/10.1016/j.matdes.2020.108977.
[72] O. Kolednik, J. Predan, G.X. Shan, N.K. Simha, F.D. Fischer, On the fracture behavior of inhomogeneous materials—A case study for elastically inhomogeneous bimaterials, Int. J. Solids Struct. 42 (2005) 605–620, https://doi.org/10.1016/j.ijsolstr.2004.06.064.
[73] O. Kolednik, J. Predan, Influence of the material inhomogeneity effect on the crack growth behavior in fiber and particle reinforced composites, Eng. Fract. Mech. 261 (2022) 108206, https://doi.org/10.1016/j.engfracmech.2021.108206.
[74] B. Cotterell, T. Pardoen, A.G. Atkins, Measuring toughness and the cohesive stress–displacement relationship by the essential work of fracture concept, Eng. Fract. Mech. 72 (2005) 827–848, https://doi.org/10.1016/j.engfracmech.2004.10.002.
[75] T. Bárány, T. Czigány, J. Karger-Kocsis, Application of the essential work of fracture (EWF) concept for polymers, related blends and composites: A review, Prog. Polym. Sci. 35 (2010) 1257–1287, https://doi.org/10.1016/j.progpolymsci.2010.07.001.
[76] B. Lauke, T. Schüller, Essential work of interfacial fracture: a method to characterise adhesion at polymer–polymer interfaces, Int. J. Adhes. Adhes. 21 (2001) 55–58, https://doi.org/10.1016/S0143-7496(00)00028-2.
[77] R.R. Deshmukh, A.R. Shetty, Comparison of surface energies using various approaches and their suitability, J. Appl. Polym. Sci. 107 (2008) 3707–3717, https://doi.org/10.1002/app.27446.
[78] F. Awaja, M. Gilbert, G. Kelly, B. Fox, P.J. Pigram, Adhesion of polymers, Prog. Polym. Sci. 34 (2009) 948–968, https://doi.org/10.1016/j.progpolymsci.2009.04.007.
[79] G. Fourche, An overview of the basic aspects of polymer adhesion. Part I: Fundamentals, Polym. Eng. Sci. 35 (1995) 957–967, https://doi.org/10.1002/pen.760351202.
[80] D.H. Kaelble, Peel Adhesion: Influence of Surface Energies and Adhesive Rheology, J. Adhes. 1 (1969) 102–123, https://doi.org/10.1080/00218466908078882.
[81] R.P. Kusy, M.J. Katz, Generalized theory of the total fracture surface energy for glassy organic polymers, Polym. J. 19 (1978) 1345–1357, https://doi.org/10.1016/0032-3861(78)90320-8.
[82] S. Flink, F.C.J.M. Van Veggel, D.N. Reinhoudt, Functionalization of self-assembled monolayers on glass and oxidized silicon wafers by surface reactions, J. Phys. Org. Chem. 14 (2001) 407–415, https://doi.org/10.1002/poc.372.
[83] X. Pei, A. Fernandes, B. Mathy, X. Laloyaux, B. Nysten, O. Riant, A.M. Jonas, Correlation between the Structure and Wettability of Photoswitchable Hydrophilic Azobenzene Monolayers on Silicon, Langmuir 27 (2011) 9403–9412, https://doi.org/10.1021/la201526u.
[84] W. Wang, M.W. Vaughn, Morphology and amine accessibility of (3-aminopropyl) triethoxysilane films on glass surfaces, Scanning 30 (2008) 65–77, https://doi.org/10.1002/sca.20097.